Strong coupling and periodic potential at the Pb/Sb(111) interface

T. Vincent,[1] S. Vlaic,[1,*] S. Pons,[1] Tianzhen Zhang,[1] H. Aubin,[1] V. S. Stolyarov,[1,2,3,4] A. S. Ksenz,[3] A. M. Ionov,[3]
S. V. Chekmazov,[3] S. I. Bozhko,[3] and D. Roditchev[1,5]

[1]*Laboratoire de Physique et d'Étude des Matériaux, ESPCI Paris, PSL Research University, CNRS,
Sorbonne Universités, UPMC Université Paris 06, 75005 Paris, France*
[2]*Moscow Institute of Physics and Technology, 141700 Dolgoprudny, Russia*
[3]*Institute of Solid State Physics, Russian Academy of Science, 142432 Chernogolovka, Russia*
[4]*Dukhov Research Institute of Automatics (VNIIA), Sushschevskaya 22, Moscow 127055, Russia*
[5]*INSP, UPMC Paris 6 and CNRS-UMR 7588, 4 place Jussieu, 75252 Paris, France*

Proximity phenomena between superconductors and topological semimetals are at the heart of the search for novel quantum states of matter. Here we show that the epitaxial interface between one- to three-atomic-layer Pb and the Sb(111) substrate has extremely high electronic transparency. As a result, Pb loses its superconducting and even its metallic properties; its electronic spectrum mimics the semimetallic density of states of Sb. Additional states arise from a threefold symmetric potential which develops at the Pb/Sb interface. Our experimental results are supported by DFT simulations which demonstrate that this potential arises from the corrugated structure of the Pb/Sb interface.

I. INTRODUCTION

The use of interface effects, between superconductors and other materials, is currently a highly used strategy to induce peculiar quantum states in solid-state matter [1–7]. Interfaces between superconductors and nontrivial topological semimetals are expected to induce unconventional superconductivity via the proximity effect [8]. Recent studies have shown that superconductivity can be induced in semimetal nanowires by the proximity effect with s-wave superconductors [9,10], and in some cases, the critical current of the nanowires can be enhanced due to the interplay at interfaces between topological semimetal surface states and spin-orbit coupling [11]. Therefore, the study of the electronic properties of superconductor/semimetal interfaces seems to be a fundamental aspect in the understanding of novel quantum properties. Here a Pb/Sb system appears very promising. Sb(111) is a good candidate to interface with a superconductor due to its nontrivial topology [12]. It has been demonstrated that it holds topological surface states [13] which are attractive not only from the fundamental point of view, such as the realization of Majorana states [8], but also for spintronic applications in the view of their robustness and the forbidden backscattering [14]. On the other hand, Pb is a good candidate to complete the interface since it is a well-known s-wave BCS superconductor with an accessible critical temperature which remains superconducting at very low thickness, down to single atomic layers [15,16], and in ultrasmall nanostructures, reaching the Anderson limit [17].

However, the realization of nontrivial superconducting states strongly depends on the density of states of the semimetal and its electronic coupling with the superconductor. The strong coupling is necessary to induce the superconducting correlations from the superconductor to the semimetal, but conversely, the semimetal could suppress the superconductivity via the inverse proximity effect in the case of strong coupling between the two materials [1]. Previous studies on Pb/highly oriented pyrolytic graphite (HOPG) [18] and Pb/InAs [17] systems revealed only a very weak capacitive coupling, which is unsuitable for efficient propagation of superconducting correlations across the interface.

In this work we report the electronic properties of ultrathin Pb single nanocrystals grown on a Sb(111) substrate. Unlike in previously reported weakly coupled Pb/HOPG [18] and Pb/InAs [17], in Pb/Sb(111) we observed a very strong electron coupling between the two subsystems. It is evidenced by two striking features: a strong modification of the density of electronic states of Pb due to the underlying Sb and a shift of the superconducting transition in the Pb nanoislands below $T_C < 1.5$ K by the strong inverse proximity effect. Moreover, we revealed the existence of a periodic threefold-symmetric potential which develops at the interface between the two materials and studied this potential in detail using scanning tunneling microscopy and spectroscopy (STM/STS), performed at 1.3 K, and density functional theory (DFT) simulations.

II. METHODS

The experiments were performed in an ultrahigh vacuum environment (base pressure $<2 \times 10^{-10}$) where the Sb(111) single crystal was mechanically cleaved at room temperature (RT). The 0.3 Pb monolayers (ML) were deposited at RT followed by a short annealing at $100\,^{\circ}$C. Using this procedure, no preferential height of the Pb nanostructures was observed.

*Corresponding author: sergio.vlaic@espci.fr

STM and STS measurements were performed at 1.3 K in the same experimental chamber with bias voltage applied to the sample. The local tunneling conductance $dI(V)/dV$ was obtained by numerical derivation of the raw $I(V, x, y)$ spectra. In the conductance maps the STM set point was fixed ($I = 200$ pA, $V = -2$ V) at each position; then the $I(V)$ curve was measured with the open feedback loop.

We have employed plane-wave DFT-based calculations using VASP [19–21] to perform the calculations of the density of states (DOS) and STM image simulations. The projector augmented-wave [22] potentials, as implemented in VASP, were used for ion-electron interactions in all the calculations. For exchange and correlation potentials, the generalized gradient approximation using the parametrization scheme of Perdew, Burke, and Ernzerhof [23,24] was employed. The so-called repeated-slab geometries [25] are employed to model the Sb(111) and Pb/Sb(111) films. A vacuum layer of about 20 Å is adopted to separate the Sb(111) slabs along the z direction in two adjacent cells. The results for fully relaxed structures are presented in this work. A converged plane-wave cutoff energy E_{cutoff} of 530 eV was used for all simulated structures. As will be shown later, a Pb overlayer on Sb(111) leads to the creation of a surface superstructure composed of 5×5 Pb unit cells on 4×4 Sb surface unit cells, requiring a large surface cell for the DFT calculations. The simulated systems are then composed of four Sb bilayers which serves as the clean substrate (we will refer to this as Sb4 in the following) and one Pb overlayer on top of Sb4. In order to make a meaningful comparison with the data available in the literature the relaxed structure of Sb(111) has been calculated for a system composed of one Sb surface unit cell and ten Sb bilayers (referred to as Sb10 in the following). The resulting structural parameters, which correspond to bulk Sb within 0.1% deviation, have been used to fix the atomic positions in the bottom bilayer in Sb4 while relaxing the rest of the system. Due to the difference of the surface unit cells for Sb4 and Sb10, we used $3 \times 3 \times 1$ and $13 \times 13 \times 1$ Monkhorst-Pack sampling grids [26], respectively, to have a comparable k-point density between all the simulations. STM images simulated using VASP in the Tersoff-Hamman [27] approach are presented as isocontours of spatial charge distribution.

III. RESULTS AND DISCUSSION

A. Topographic and average electronic properties

With the chosen sample preparation conditions Pb islands grow in a Volmer-Weber mode on top of a wetting layer (WL), as shown in Fig. 1(a). The islands are 5–10 nm wide and 2–5 ML high; most of them have a regular (triangular, hexagonal) shape. In order to probe the interface Pb/Sb properties we focused on the thinner islands, such as those appearing in the central region of Fig. 1(a). The detailed shape of these islands, linked by a WL, is reported in Fig. 1(b). The three islands have different thicknesses, as presented by the line profiles in Fig. 1(c). All edges of the islands are oriented along the crystallographic directions of the substrate, as indicated by the inset of Fig. 1(b), which shows the atomic resolution image of the neighboring naked Sb substrate. The topmost large island, the triangular island, and the hexagonal one are, respectively,
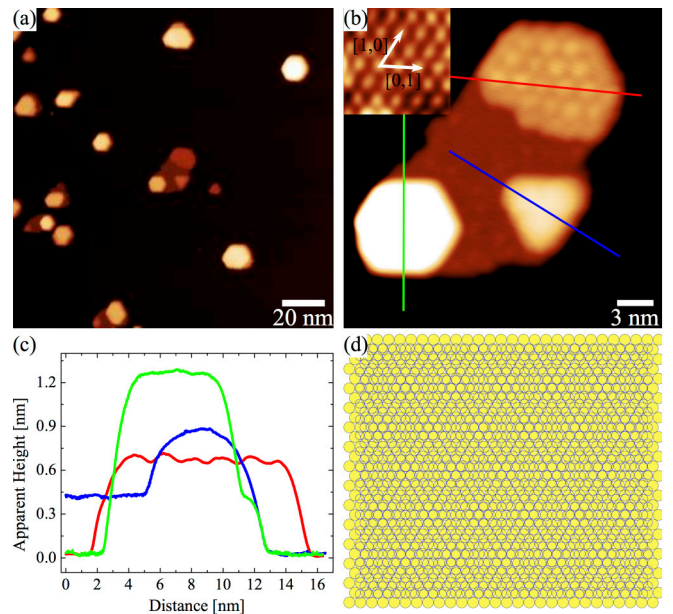

FIG. 1. (a) Large-scale topography image ($I = 200$ pA, $V = -2$ V) of Pb nanostructures on Sb(111). (b) High-resolution topography image of the selected nanostructures at the center of (a). One can identify the moiré island, a triangular island, and a hexagonal island on top of the wetting layer. Inset: Atomic resolution image of the clean Sb(111) surface with the [1,0] and [0,1] surface lattice vectors indicated by white arrows. (c) Line profiles along the three lines in (b). (d) Sketch of the moiré superstructure arising from the superposition of Pb atoms (blue open circles, $a_{Pb(111)} = 3.5$ Å) and Sb atoms (yellow solid circles, $a_{Sb(111)} = 4.3$ Å).

1, 2, and 4 ML higher than the WL. The thinnest (topmost) island presents a moiré pattern (in the following we will refer to this nanostructure as the moiré island). A triangular island just 1 ML thicker already shows no moiré pattern (although weak periodic electronic modulations remain, as we show later). In general, thicker islands do not reveal any measurable moiré pattern in topographic STM images. This observation points towards the interfacial origin of the moiré pattern in the Pb/Sb(111) system.

In the moiré island the periodicity of the moiré pattern is about 1.80 ± 0.15 nm, which matches five Pb and four Sb interatomic distances (3.5 and 4.3 Å, respectively, considering free Pb(111) and Sb(111) surfaces [28,29]). It has to be noted that in several moiré islands we measured some deformations of the moiré superstructure with respect to a perfect hexagonal lattice, probably due to distortions induced by edges. The expected moiré pattern is presented in Fig. 1(d). Thus, similar to the cases of Pb/Si(111) [30] and Pb/InAs(111) [17], Pb nanostructures tend to expose the {111} facets and recover their bulk lattice constants already at very low thickness, thus producing a superperiodic moiré pattern.

Figure 2 shows the surface-averaged dI/dV spectra, proportional to the DOS in the first approximation, acquired on the naked Sb substrate (black line), on the moiré island (red line), and on the triangular island (blue line). Surprisingly, aside from the two peaks appearing at -1.5 and -1 V specific to the naked Sb(111) surface, the three spectra appear very
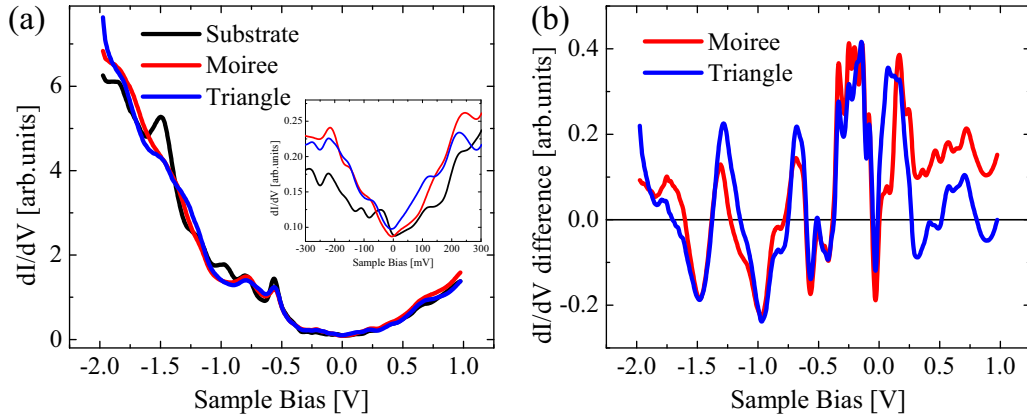
FIG. 2. (a) Average dI/dV spectra on the clean substrate (black), the moiré island (red), and the triangular island (blue). Inset: zoom around the Fermi level. (b) Normalized dI/dV difference between the islands and the substrate, defined as $(dI/dV_{islands} - dI/dV_{substrate})/dI/dV_{substrate}$.

similar. Precisely, Sb presents a bump in dI/dV around -600 mV and a clear semimetallic behavior represented by a strong reduction in the dI/dV intensity around the Fermi level [see the inset in Fig. 2(a)]. This result is in good agreement with previous angle-resolved photoemission spectroscopy and STS measurements on Sb(111) [31,32]. Surprisingly, the tunneling dI/dV spectra measured on the Pb islands have exactly the same overall trend: U-shaped spectra with a minimum at the Fermi level. The differences with respect to dI/dV of the substrate [defined as $(dI/dV_{islands} - dI/dV_{substrate})/dI/dV_{substrate}$] do not exceed 20% in most parts of the spectra, the highest difference being measured near the Fermi level [Fig. 2(b)]. Although the dI/dV signal of Pb islands near E_F is up to 40% higher than in Sb(111), we did not observe any signature of the superconducting gap at zero bias. The absence of the superconducting gap in the spectra measured at 1.3 K is proof of a significant reduction of the critical temperature in the thinnest Pb islands, even if we cannot assert full suppression of superconductivity there. This suppression becomes possible owing to the inverse proximity effect of the Sb substrate. Therefore, both the overall shape of the tunneling conductance and the absence of the superconducting gap in Pb islands are evidence of strong coupling between the electronic structures of Pb islands and the substrate. The latter imposes its own electronic structure and dominates the electronic properties of Pb.

B. Local density of states: Moiré island

A closer look at the spatially resolved electronic properties of the Pb nanostructures helps to elucidate the effect of the Pb/Sb interface. Figure 3(a) shows the spectroscopic dI/dV map recorded at -540 mV on the moiré island. Although topographic corrugations are compensated at each location before the spectroscopy is taken, the superstructure is clearly visible, showing the periodic reorganization of the local DOS (LDOS) in the moiré island and therefore the existence of an electronic potential. The orientation of the dI/dV modulations follows the substrate crystallographic directions as depicted by Fig. 3(a): The moiré top positions (black circles) are aligned with the [1,0] axis, indicated by the white arrow.

Starting from one top position, one can therefore identify two neighboring hollow sites in the superstructure oriented at 30° clockwise (gray circles, hollow cites C) and counterclockwise (blue circles, hollow cites A) with respect to the [1,0] direction. The comparison of the dI/dV corresponding to these two locations gives information about the in-plane symmetry of the potential. The spectra measured in the top position and in the two hollow sites, A and C, are reported in the inset in Fig. 3(b). Besides the dI/dV difference between top and hollows sites, which gives rise to the contrast in STS maps, the inset in Fig. 3(b) demonstrates that the two hollow positions are inequivalent, a signature of a threefold symmetry of the superpotential. The electronic nature of the phenomenon becomes even more evident when examining the evolution of the dI/dV contrast with the bias voltage, defined as $(dI/dV_{top} - dI/dV_{hollow})/dI/dV_{island}$ [Fig. 3(c)]. One can identify two contrast inversions that occur at -1.56 and -0.74 V, as demonstrated by two STS maps acquired at -1.2 and 0.5 V, shown as insets. This contrast inversion of the moiré pattern ensures the electronic contribution to the observed superstructure as in the cases, for example, of graphene on metals [33], Mn on Ag(111) [34], and the periodic potential induced in vicinal surfaces [35]. As expected from the previous discussion on the potential symmetry, the contrast evolution behaves differently, in terms of intensity, for the two hollow positions, A and C (shown in blue and gray, respectively). The normalized dI/dV difference, defined as $(dI/dV_{region} - dI/dV_{substrate})/dI/dV_{substrate}$, shows in Fig. 3(b) that the two hollow parts are characterized by slightly different signals, and both of them follow that of the naked substrate. On the contrary, dI/dV at the top parts of the moiré superstructure presents the highest variation with respect to dI/dV of Sb(111) in the vicinity of the Fermi level. This analysis demonstrates that the potential responsible for the modulations is threefold symmetric and that the top parts of the moiré island behave differently with respect to the hollow ones, which are mainly dominated by the substrate behavior. However, this does not enable one to determine the microscopic origin of the potential, which could originate from both the structural corrugations in the island and the Pb/Sb interface potential.
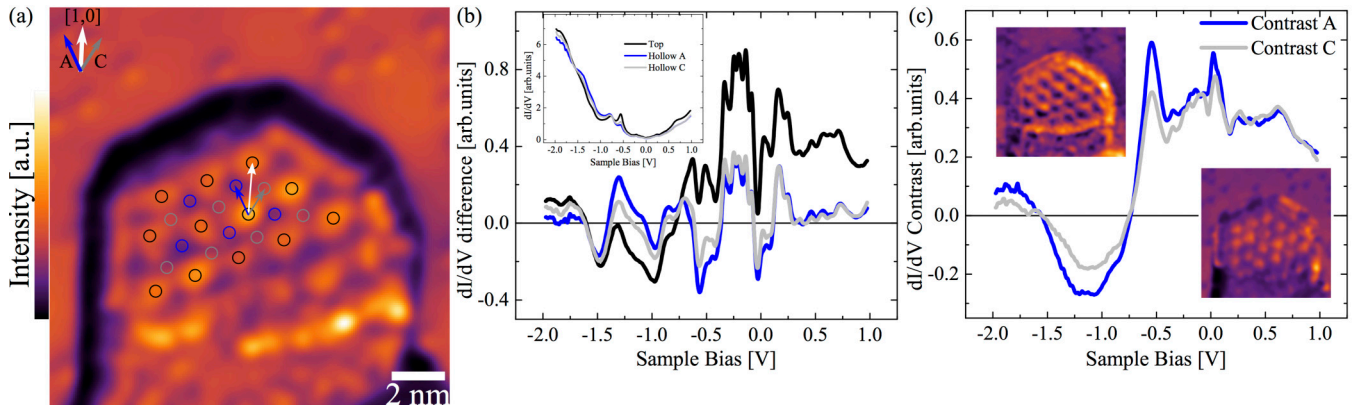
FIG. 3. (a) Scanning tunneling spectroscopy image of the moiré island at -0.54 V. The top parts of the superstructure (black circles) are aligned along the substrate crystallographic directions. The blue and gray circles identify the inequivalent hollow parts rotated counterclockwise (A) and clockwise (C) with respect to the [1,0] direction. (b) Normalized difference spectra, defined as $(dI/dV_{region} - dI/dV_{substrate})/dI/dV_{substrate}$, of the three regions indicated in (a). Inset: dI/dV spectra of the top (black), hollow A (blue), and hollow C (gray) sites of the island. (c) Contrast evolution, defined as $(dI/dV_{top} - dI/dV_{hollow})/dI/dV_{island}$, as a function of the bias voltage. Two contrast inversions are visible at -1.56 and -0.74 V. Insets: dI/dV map at -1.2 V (top left) and dI/dV map at 0.5 V (bottom right).

C. Local density of states: Triangular island

The definitive proof of the Pb/Sb interface origin of the superpotential comes from the analysis of the STS maps of the triangular island. In this island the topographic STM images [Fig. 1(b)] do not show any sign of modulation, thus excluding any top layer corrugation. However, STS maps revealed the existence of a weak periodic pattern in the island (Fig. 4). To clearly identify the tops and hollow positions of this weak electronic modulation we made averaged dI/dV maps in the energy window from -0.65 to -0.4 V, which corresponds to the contrast peak in Fig. 3(c). The averaged STS map is presented in Fig. 4(a). The contrast there has been artificially enhanced in order to highlight the periodic modulations. Although the signal is weak, we could clearly identify the hexagonal pattern aligned with the crystallographic directions of the substrate (white arrows). It can immediately be seen that stronger distortions of the pattern, with respect to the case of the moiré island in Fig. 3(a), are present due to the reduced lateral size (≈ 6 nm) of the island. The periodicity in this case is 1.55 ± 0.25 nm, which still matches five Pb and four Sb interatomic distances at the Pb/Sb interface. As in the case of the moiré island, we marked the top, hollow A, and hollow C sites with black, blue, and gray circles. We noticed a high dI/dV signal measured at the bottom right corner of the triangle, which is probably due to the presence of defects. To make a meaningful comparison with the STS data acquired on the moiré island we excluded this part from our analysis. The average spectra of the three constituents of the periodic dI/dV pattern of the triangular island are reported in Fig 4(b). In this case the differences are much smaller but still appreciable, mainly in the region around -0.54 V. The contrast evolution is reported in Fig. 4(c). The behavior is similar to the case of the moiré island [shown as dashed lines in Fig. 4(c)] but with a reduced intensity. Two contrast inversion positions are located almost at the same energies, and higher contrast is visible in the -0.54 and 0 V regions for the hollow A sites. The behavior of the contrast is different for the two hollow sites, as expected for a threefold-symmetric potential.

The normalized difference spectra, reported in Fig. 4(d), also resemble, but with reduced intensity, the results obtained for the moiré island. Thus, despite the intensity difference, the periodic electronic modulations identified in the moiré and triangular islands behave in a very similar way, and thus, they certainly have a common Pb/Sb interface origin.
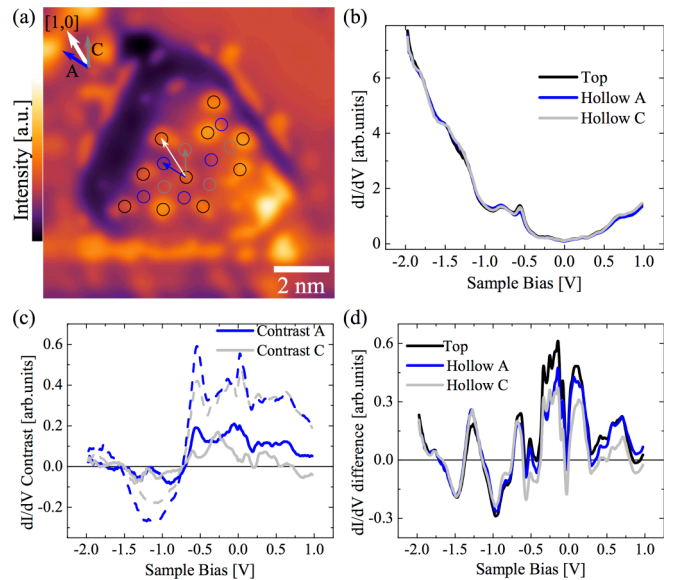

FIG. 4. (a) Averaged scanning tunneling spectroscopy map in the energy window from -0.65 to -0.4 V of the triangular island. The top parts of the superstructure (black circles) are aligned along the substrate crystallographic directions. The blue and gray circles identify the inequivalent hollow parts rotated counterclockwise (A) and clockwise (C) with respect to the [1,0] direction. The contrast has been enhanced to highlight dI/dV periodicity. (b) dI/dV spectra of the top (black), hollow A (blue), and hollow C (gray) sites of the island. (c) Contrast evolution, defined as $(dI/dV_{top} - dI/dV_{hollow})/dI/dV_{island}$, as a function of the bias voltage. (d) Normalized difference spectra, defined as $(dI/dV_{region} - dI/dV_{substrate})/dI/dV_{substrate}$, of the three regions indicated in (a).
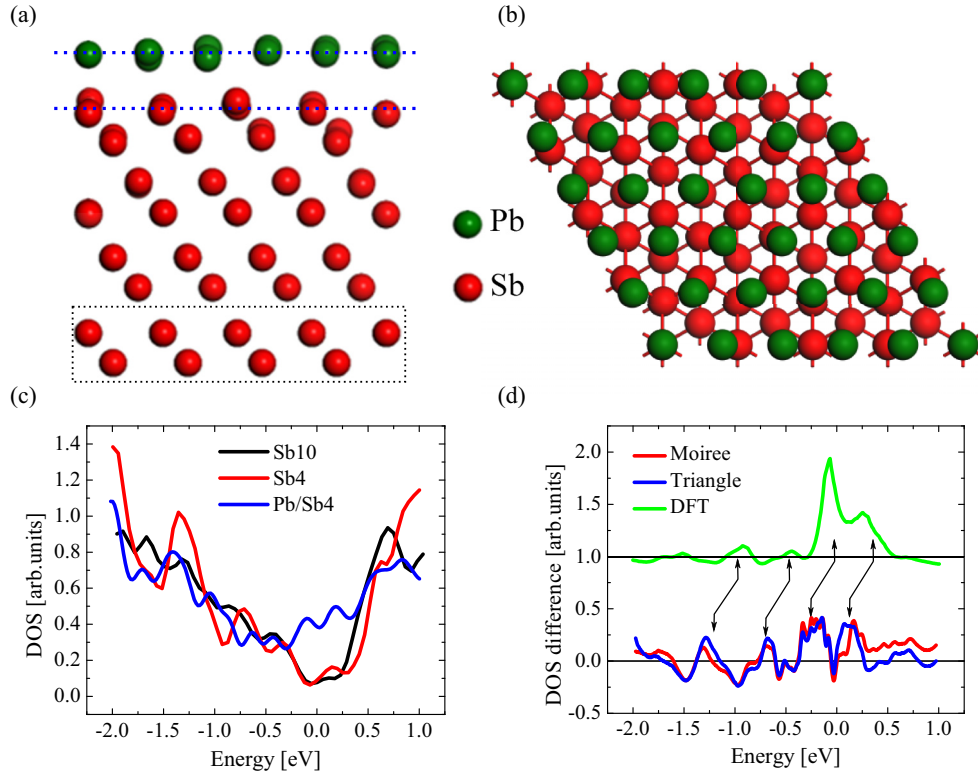
FIG. 5. (a) Side and (b) top views of the system used for DFT simulations composed of a monolayer of Pb atoms (green) over four bilayers of Sb atoms (red). The black dashed rectangle highlights the last Sb bilayer whose atomic position has been fixed as explained in the text. Blue dashed lines represent the average vertical positions of the Pb and top Sb atomic layers. (c) Simulated density of states of the bare substrate composed of ten Sb bilayers (black), four Sb bilayers (red), and the Pb monolayer over four Sb bilayers (blue). (d) Simulated DOS difference, defined as $(DOS_{Pb/Sb4} - DOS_{Sb4})/DOS_{Sb4}$ (green, shifted for clarity), and the differential dI/dV spectra as reported in Fig. 2(b).

D. DFT calculations

To elucidate the prominent role of the Pb/Sb interface in the periodic modulation of the LDOS we performed DFT simulations of one atomic Pb layer adsorbed on the Sb(111) surface. We first proceeded with the calculations of the relaxed Sb(111) structure using the Sb10 system described in Sec. II. Sb has the rhombohedral A7 crystal structure with space group $R\bar{3}m$. The resulting optimized structure corresponds to the rhombohedral crystal structure of Sb with a lattice constant of 4.587 Å and with an angle of 57.010° between the axes of the rhombohedron. The unit cell contains two atoms located along the main diagonal of the rhombohedron. The coordinates of these atoms within the unit cell are (0.233, 0.233, 0.233) and (0.767, 0.767, 0.767), in agreement with the data reported in Ref. [36]. Including spin-orbit coupling (SOC) in the calculations modifies the lattice constant less than 0.1% and, in the energy range we are interested in, has a negligible effect on the Sb DOS. Therefore, SOC has been neglected in the following. In order to simulate a system as close as possible to that evidenced by experimental measurements we expanded the surface unit cell to the moiré supercell (5×5 Pb unit cells over 4×4 Sb surface unit cells) while reducing the number of bilayers in the Sb substrate to four (see Sb4 in Sec. II). The lattice parameters obtained in the simulation of the Sb10 system have been used to fix the atomic positions of the bottom bilayer of Sb4 and Pb/Sb4, whose schematic structures are reported in Figs. 5(a) and 5(b), while the rest

of the structure has been relaxed. To justify the reduction of the substrate thickness we show in Fig. 5(c) a comparison between the DOSs of Sb10 and Sb4 system, whose qualitative trends are in agreement. For comparison the DOS of Pb/Sb4 is also shown. The relaxed Sb10 and Sb4 structures show no corrugation on the Sb surface, while, upon Pb adsorption, a reorganization of surface atoms takes place. Both Pb and Sb top-layer atoms rearrange their vertical position inside the unit cell, producing a maximum displacement with respect to the average position of about 0.3 Å (0.6 Å corrugation) as schematically reported in Fig. 5(a) (blue dashed lines). This value is in agreement with the corrugation of the moiré island reported in Fig 1. In-plane variation of the atomic positions does not exceed 0.1 Å for all the atoms in the Pb/Sb4 system. The DOS difference between Pb/Sb4 and the bare Sb4 substrate is presented in Fig 5(d) (green, shifted for clarity) together with the averaged differential dI/dV of the moiré and triangular islands already shown in Fig. 2(b). Despite the few hundreds of meV energy shift, striking similarities are seen. In the negative-bias region the differential DOS shows oscillations with a 500–600 meV period with an enhanced intensity close to zero.

To finally demonstrate the electronic origin of the measured dI/dV modulations we show two simulated STM images for two different energies in Fig. 6(a) (-0.85 eV) and Fig. 6(b) (0.15 eV), showing a drastic contrast inversion. Line profiles taken along the blue lines in Figs. 6(a) and 6(b) are
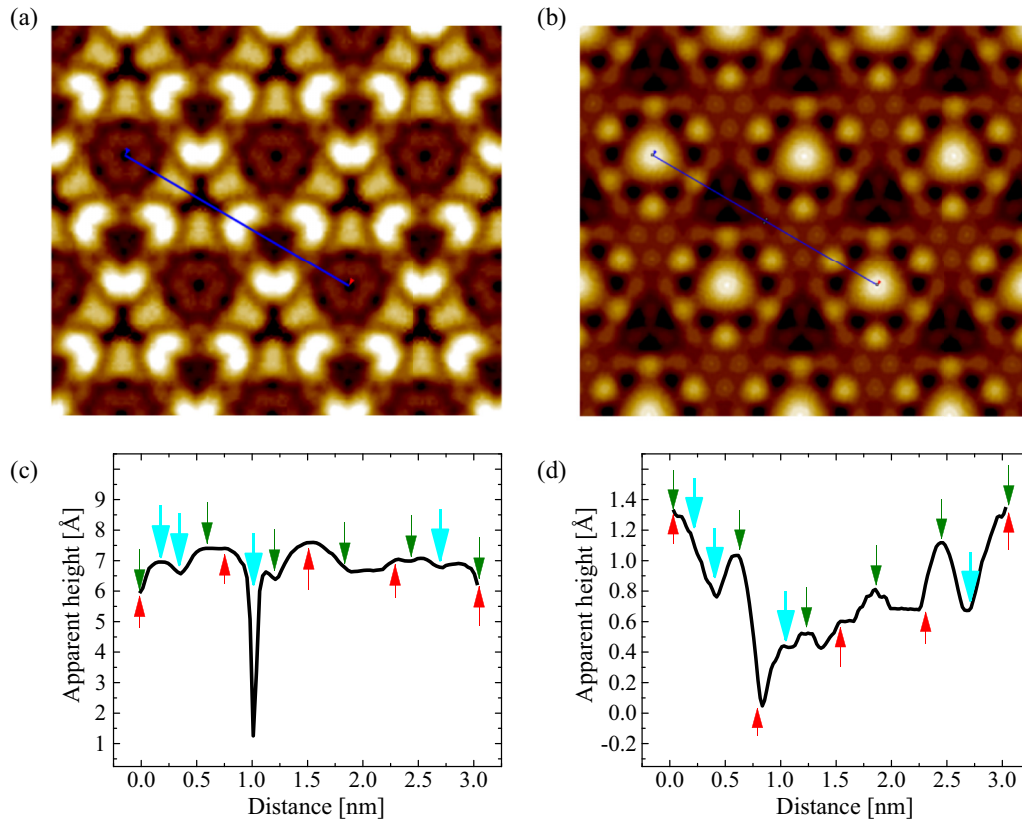
FIG. 6. (a) and (b) Simulated STM images at −0.85 and 0.15 eV, respectively, showing contrast inversion. (c) and (d) Apparent height profile along the blue lines in (a) and (b), respectively. Red (green) arrows indicate the Sb (Pb) atomic position in the respective top layer, while the blue arrows highlight specific features in the line profile which do not correspond to any atom.

reported in Figs 6(c) and 6(d), respectively. Here the red (green) arrows indicate the Sb (Pb) atomic position in the respective top layer, while the blue arrows highlight specific features in the line profile which do not correspond to any atom. Both images and lines profiles prove that the positions of hills and valleys in the STM images are strongly dependent on the applied bias voltage and therefore on the probed energy. These theoretical results demonstrate that the Pb/Sb(111) interface

structure appears corrugated on both the Pb and Sb top layers, leading to a threefold-symmetric potential which can be accounted for by the observed modulation of the density of states.

Insight into the strength of the potential is given by Fig. 7. To reveal charge transfer induced by the Pb and Sb interactions at the interface, we calculated the charge distribution for Pb/Sb4, one Pb layer, and the Sb4 structure [supercells
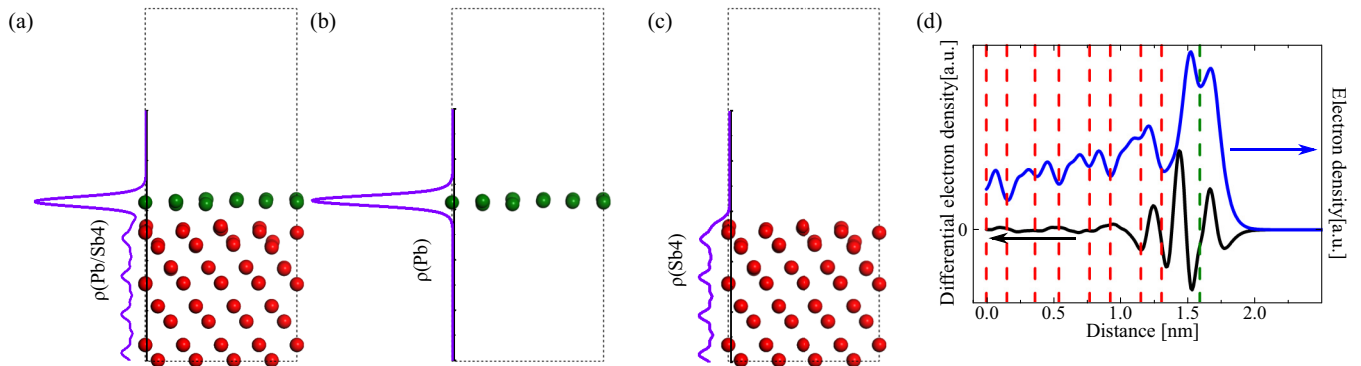

FIG. 7. (a)–(c) Supercells of Pb/Sb4, Pb, and Sb4 structures used in simulations. Charge densities ρ(Pb/Sb4), ρ(Sb4), and ρ(Pb) integrated for a plane parallel to the surface as a function of the distance from the Sb surface are presented on the left side of each structure in violet. (d) Difference of electron density distribution ρ(Pb/Sb4) − ρ(Sb4) − ρ(Pb) (black curve) and partial charge density distribution (blue curve), integrated from the Fermi level to −0.5 eV, presented as a function of the distance from the Sb bottom layer. Red and green dashed lines indicate the average positions of the Sb and Pb planes, respectively.

schematically imaged in Figs. 7(a)–7(c); all supercells have the same volume]. Pb and Sb4 supercells were obtained from fully relaxed Pb/Sb4 by removing Sb and Pb atoms, respectively. The charge densities $\rho(\text{Pb/Sb4})$, $\rho(\text{Sb4})$, and $\rho(\text{Pb})$ were integrated for a plane parallel to the surface as a function of the distance from the Sb4 bottom layer and are indicated in violet to the left of the respective structure. The variation of the planar average of the difference of the electron density distribution $[\rho(\text{Pb/Sb4}) - \rho(\text{Sb4})]/\rho(\text{Pb})$ is presented in Fig. 7(d) (black curve) together with the calculated partial electron density, integrated from the Fermi energy to -0.5 eV (blue curve). The red lines represents the average vertical position of the Sb planes (Sb4 substrate), while the green one shows the position of the Pb layer. As expected, the electron density is much stronger in the Pb layer; it decays slowly towards the bulk of the substrate. Unfortunately, due to the reduced number of Sb slabs used in the calculations, it is not possible to quantitatively measure the decay length. The difference of the electron density distribution shows a strong reorganization of electrons at the Pb/Sb interface compared to isolated Pb and Sb4, which demonstrates the existence of a strong electronic coupling between the two materials. Indeed, the actual structure of the interface atomic layer could be composed of a PbSb eutetic which forms at about $250\,^\circ$C in bulk material [37]. Therefore, at surfaces, an intermixing of Pb and Sb atoms could be induced at lower temperature (i.e., annealing temperature), resulting in the formation of an alloy interface between pure Sb and Pb. Nevertheless, the solubility of the two materials is rather low at $100\,^\circ$C [37]; therefore, we do not expect that our nanostructure is composed of a PbSb alloy. Moreover, our DFT simulations reproduce qualitatively the experimental results considering no intermixing.

IV. CONCLUSIONS

In conclusion we studied the electronic properties of Pb nanoislands grown *in situ* on a Sb(111) substrate. We revealed a strong modification of the density of states of Pb due to the electronic coupling to a Sb bath affecting the whole studied energy range and observed the suppression of conventional superconductivity in Pb below 1.5 K. We found that the Pb/Sb corrugated interface gives rise to an additional threefold electronic potential, resulting in $\sim$1.8-nm periodic modulations of the electronic density. The amplitude of these modulations rapidly vanishes with increasing Pb-island thickness. Owing to the established strong electronic coupling the Pb/Sb(111) system is a promising candidate for realizing nontrivial superconducting correlations. To reveal them and to examine the role played by the observed superpotential further STS experiments have to be conducted at ultralow temperature.

[1] A. I. Buzdin, Rev. Mod. Phys. **77**, 935 (2005).

[2] H. le Sueur, P. Joyez, H. Pothier, C. Urbina, and D. Esteve, Phys. Rev. Lett. **100**, 197002 (2008).

[3] L. Serrier-Garcia, J. C. Cuevas, T. Cren, C. Brun, V. Cherkez, F. Debontridder, D. Fokin, F. S. Bergeret, and D. Roditchev, Phys. Rev. Lett. **110**, 157003 (2013).

[4] Y.-J. Doh, J. A. van Dam, A. L. Roest, E. P. A. M. Bakkers, L. P. Kouwenhoven, and S. De Franceschi, Science **309**, 272 (2005).

[5] P. Jarillo-Herrero, J. A. van Dam, and L. P. Kouwenhoven, Nature (London) **439**, 953 (2006).

[6] S. Nadj-Perge, I. K. Drozdov, J. Li, H. Chen, S. Jeon, J. Seo, A. H. MacDonald, B. A. Bernevig, and A. Yazdani, Science **346**, 602 (2014).

[7] J.-F. Ge, Z.-L. Liu, C. Liu, C.-L. Gao, D. Qian, Q.-K. Xue, Y. Liu, and J.-F. Jia, Nat. Mater. **14**, 285 (2015).

[8] J. Linder, Y. Tanaka, T. Yokoyama, A. Sudbø, and N. Nagaosa, Phys. Rev. Lett. **104**, 067001 (2010).

[9] S. Li, N. Kang, D. X. Fan, L. B. Wang, Y. Q. Huang, P. Caroff, and H. Q. Xu, Sci. Rep. **6**, 24822 (2016).

[10] S. Sangiao, L. Casado, L. Morellón, M. R. Ibarra, and J. M. D. Teresa, J. Phys. D **50**, 12LT02 (2017).

[11] C. Li, A. Kasumov, A. Murani, S. Sengupta, F. Fortuna, K. Napolskii, D. Koshkodaev, G. Tsirlina, Y. Kasumov, I. Khodos, R. Deblock, M. Ferrier, S. Guéron, and H. Bouchiat, Phys. Rev. B **90**, 245427 (2014).

[12] P. Roushan, J. Seo, C. V. Parker, Y. S. Hor, D. Hsieh, D. Qian, A. Richardella, M. Z. Hasan, R. J. Cava, and A. Yazdani, Nature (London) **460**, 1106 (2009).

[13] J. Seo, P. Roushan, H. Beidenkopf, Y. S. Hor, R. J. Cava, and A. Yazdani, Nature (London) **466**, 343 (2010).

[14] D. Pesin and A. H. MacDonald, Nat. Mater. **11**, 409 (2012).

[15] C. Brun, T. Cren, V. Cherkez, F. Debontridder, S. Pons, D. Fokin, M. C. Tringides, S. Bozhko, L. B. Ioffe, B. L. Altshuler, and D. Roditchev, Nat. Phys. **10**, 444 (2014).

[16] T. Zhang, P. Cheng, W.-J. Li, Y.-J. Sun, G. Wang, X.-G. Zhu, K. He, L. Wang, X. Ma, X. Chen, Y. Wang, Y. Liu, H.-Q. Lin, J.-F. Jia, and Q.-K. Xue, Nat. Phys. **6**, 104 (2010).

[17] S. Vlaic, S. Pons, T. Zhang, A. Assouline, A. Zimmers, C. David, G. Rodary, D. Roditchev, and H. Aubin, Nat. Commun. **8**, 14549 (2017).

[18] C. Brun, K. H. Müller, I.-P. Hong, F. Patthey, C. Flindt, and W.-D. Schneider, Phys. Rev. Lett. **108**, 126802 (2012).

[19] G. Kresse and J. Furthmüller, Phys. Rev. B **54**, 11169 (1996).

[20] G. Kresse and J. Hafner, Phys. Rev. B **47**, 558 (1993).

[21] G. Kresse and J. Furthmüller, Comput. Mater. Sci. **6**, 15 (1996).

[22] P. E. Blöchl, Phys. Rev. B **50**, 17953 (1994).

[23] J. P. Perdew and Y. Wang, Phys. Rev. B **45**, 13244 (1992).

[24] J. P. Perdew, K. Burke, and M. Ernzerhof, Phys. Rev. Lett. **77**, 3865 (1996).

[25] F. Bechstedt, *Principles of Surface Physics* (Springer, Berlin, 2003).

[26] H. J. Monkhorst and J. D. Pack, Phys. Rev. B **13**, 5188 (1976).

[27] J. Tersoff and D. R. Hamann, Phys. Rev. B **31**, 805 (1985).

[28] H. Pan and X.-S. Wang, Nanoscale Res. Lett. **10**, 334 (2015).

[29] X. Ma, P. Jiang, Y. Qi, J. Jia, Y. Yang, W. Duan, W.-X. Li, X. Bao, S. B. Zhang, and Q.-K. Xue, Proc. Natl. Acad. Sci. USA **104**, 9204 (2007).

[30] K. Budde, E. Abram, V. Yeh, and M. C. Tringides, Phys. Rev. B **61**, R10602 (2000).

[31] K. Sugawara, T. Sato, S. Souma, T. Takahashi, M. Arai, and T. Sasaki, Phys. Rev. Lett. **96**, 046411 (2006).

[32] A. Soumyanarayanan, M. M. Yee, Y. He, H. Lin, D. R. Gardner, A. Bansil, Y. S. Lee, and J. E. Hoffman, arXiv:1311.1758.

[33] E. N. Voloshina, E. Fertitta, A. Garhofer, F. Mittendorfer, M. Fonin, A. Thissen, and Y. S. Dedkov, Sci. Rep. **3**, 1072 (2013).

[34] J. Kliewer, R. Berndt, and S. Crampin, New J. Phys. **3**, 22 (2001).

[35] C. Didiot, Y. Fagot-Revurat, S. Pons, B. Kierren, C. Chatelain, and D. Malterre, Phys. Rev. B **74**, 081404 (2006).

[36] C. Barrett, P. Cucka, and K. Haefner, Acta Crystallogr. **16**, 451 (1963).

[37] A. P. S. Ashtakala and C. Bale, Bull. Alloy Phase Diagrams **2**, 86 (1981).